Molecular Dynamics Simulations of Human Prion Protein: Importance of Correct Treatment of Electrostatic Interactions

J. Zuegg and J. E. Gready*

Division of Biochemistry and Molecular Biology, John Curtin School of Medical Research, Australian National University, P.O. Box 334, Canberra, ACT 2601, Australia

Received June 25, 1999; Revised Manuscript Received August 13, 1999

ABSTRACT: Molecular dynamics simulations have been used to investigate the dynamical and structural behavior of a homology model of human prion protein *Hu*PrP(*90*−*230*) generated from the NMR structure of the Syrian hamster prion protein *Sh*PrP(*90*−*231*) and of *Sh*PrP(*90*−*231*) itself. These PrPs have a large number of charged residues on the protein surface. At the simulation pH 7, *Hu*PrP(*90*−*230*) has a net charge of −1 eu from 15 positively and 14 negatively charged residues. Simulations for both PrPs, using the AMBER94 force field in a periodic box model with explicit water molecules, showed high sensitivity to the correct treatment of the electrostatic interactions. Highly unstable behavior of the structured region of the PrPs (*127*−*230*) was found using the truncation method, and stable trajectories could be achieved only by including all the long-range electrostatic interactions using the particle mesh Ewald (PME) method. The instability using the truncation method could not be reduced by adding sodium and chloride ions nor by replacing some of the sodium ions with calcium ions. The PME simulations showed, in accordance with NMR experiments with *Sh*PrP and mouse PrP, a flexibly disordered N-terminal part, PrP(*90*−*126*), and a structured C-terminal part, PrP(*127*−*230*), which includes three α-helices and a short antiparallel β-strand. The simulations showed some tendency for the highly conserved hydrophobic segment PrP(*112*−*131*) to adopt an α-helical conformation and for helix C to split at residues 212−213, a known disease-associated mutation site (Q212P). Three highly occupied salt bridges could be identified (E146/D144↔R208, R164↔D178, and R156↔E196) which appear to be important for the stability of PrP by linking the stable main structured core (helices B and C) with the more flexible structured part (helix A and strands A and B). Two of these salt bridges involve disease-associated mutations (R208H and D178N). Decreased PrP stability shown by protein unfolding experiments on mutants of these residues and guanidinium chloride or temperature-induced unfolding studies indicating reduced stability at low pH are consistent with stabilization by salt bridges. The fact that electrostatic interactions, in general, and salt bridges, in particular, appear to play an important role in PrP stability has implications for PrP structure and stability at different pHs it may encounter physiologically during normal or abnormal recycling from the pH neutral membrane surface into endosomes or lysomes (acidic pHs) or in NMR experiments (5.2 for *Sh*PrP and 4.5 for mouse PrP).

Prion protein (PrP)[1] is associated with an unusual class of neurodegenerative diseases, which include scrapie in sheep, bovine spongiform encephalopathy (BSE) in cattle, and kuru, Creutzfeldt−Jacob disease (CJD), Gerstmann−Sträussler−Scheinker syndrome (GSS), and fatal familiar insomnia (FFI) in humans (*1*−*3*). According to the *protein only* hypothesis (*1*, *4*, *5*) the disease is caused by an abnormal form of the 250 amino acid long PrP, which accumulates in plaques in the brain. This disease-associated form of PrP (PrP^{Sc}) differs from the normal cellular form (PrP^{C}) only in its three-dimensional structure, and FTIR and CD spectra indicate that it has a significantly increased content of β-sheet conformation compared with PrP^{C} (*6*, *7*).

PrP^{C} is a secreted cell surface glycoprotein with still unknown function, which cycles between the cell surface and endocytic compartments (*8*, *9*). The accumulation of PrP^{Sc} occurs in late endosomes and lysosomes (*10*). The conformational change between PrP^{C} and PrP^{Sc} in animals and humans is strongly associated with mutations in the PrP gene and leads to a protease-resistant remnant consisting of residues 90−231, which appears to be the minimum unit correlated with infectivity. As shown in Figure 1, 17 disease-associated mutations are known so far for humans (*3*, *11*−*14*), most of which occur within the C-terminal part of PrP. It has been proposed that formation of PrP^{Sc} is caused by a self-replication effect (*5*) and that this process is increased by these disease-associated mutations in the PrP gene. Two different kinetic models have been proposed. In the first model, the rate-limiting step would be the irreversible autocatalytic conversion of the monomeric PrP^{C} to a monomeric PrP^{Sc} subunit, followed by a fast oligomerization of

* To whom correspondence should be addressed: tel, 61-2-62798304; fax, 61-2-62490415; e-mail, jill.gready@anu.edu.au.

[1] Abbreviations: PrP, prion protein; *Hu*PrP, human prion protein; *Mo*PrP, murine prion protein; *Sh*PrP, Syrian hamster prion protein; PME, particle mesh Ewald.

10.1021/bi991469d CCC: $18.00
Published on Web 10/02/1999

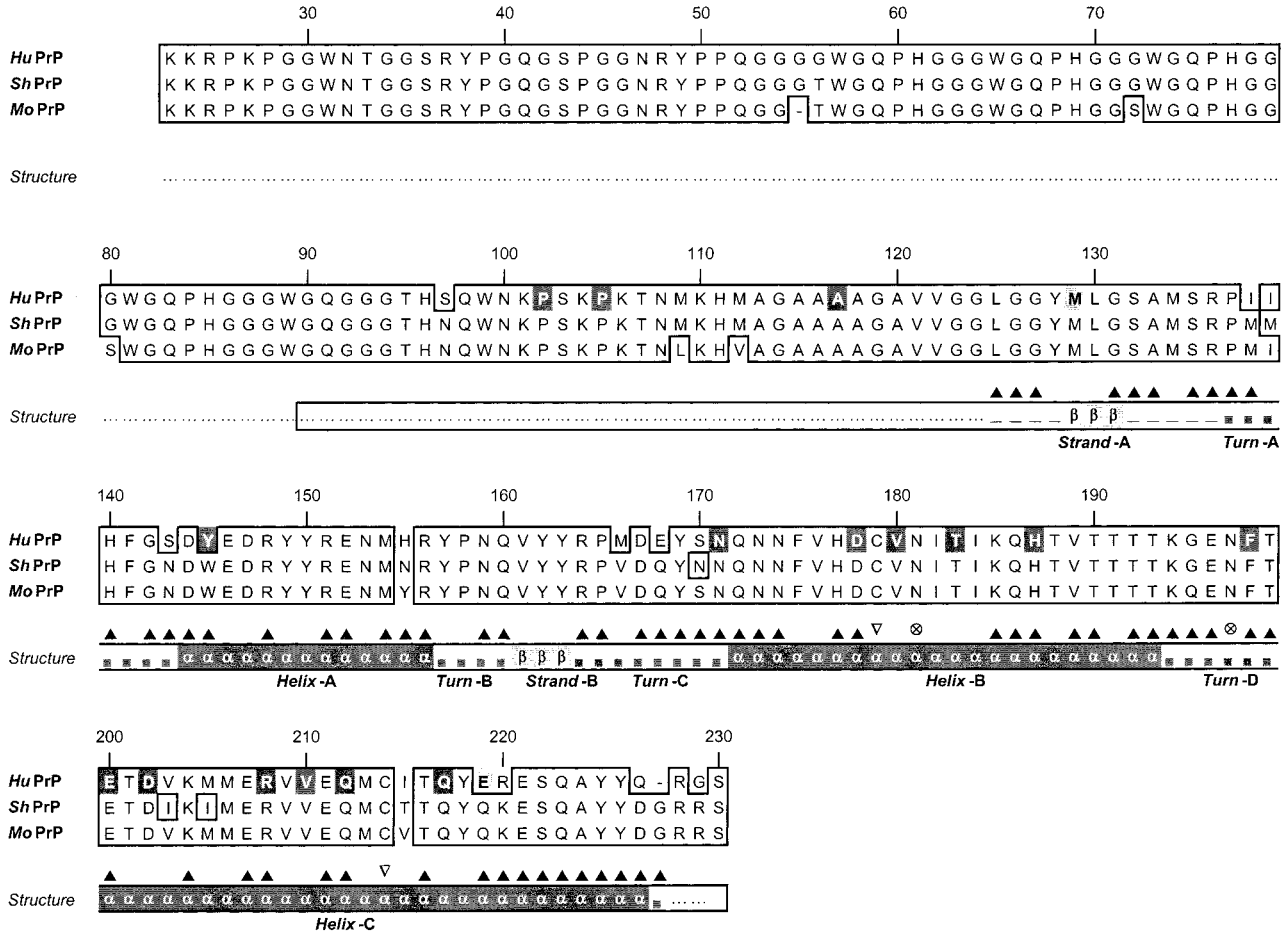

FIGURE 1: Alignment of the amino acid sequences of *Hu*PrP, *Sh*PrP, and *Mo*PrP with secondary structure information. The amino acid residues in black boxes are mutation sites known to be associated with inherited forms of PrP diseases in humans [CJD, D178N:129V (*3*), V180I (*3*), T183A (*3*), E200K (*3*), R208H (*3*), V210I (*3*), and M232R (*3*); GSS, P102L (*3*), P105L (*3*), A117V (*3*), Y145Stop (*3*), H187R (*14*), F198S (*3*), D202N (*13*), Q212P (*13*), and Q217R (*3*); FFI, D178N:129M (*3*); schizophrenia, N171S (*12*)], while in light gray boxes residues involved in some polymorphisms influencing these diseases are shown [M129V (*3*), E219K (*11*)]. The amino acid numbering is according to *Hu*PrP. The boxes denote identical amino acids among the three sequences. The structure information includes the secondary structure elements (α for α-helices, *β* for *β*-sheets, and ■ for turns) from the NMR structure of *Sh*PrP(90−231) (*29*). In addition, the dotted line (...) identifies the *flexibly* disordered part, the solid line (—) the *structured* part, and ▲ the exposed residues. The ⊗ denotes the two *N*-glycosylation sites of *Hu*PrP and ▽ the two cysteines involved in the disulfide bridge. The boxed region denotes the part of *Hu*PrP which has been included in the models, i.e., residues 90−230.

the subunits (*5*). This model has been questioned recently by simulations of the kinetics of prion formation (*15*). In the second model, a fast equilibrium between monomeric PrP^{C} and a monomeric PrP^{Sc} precursor is proposed, with the rate-limiting step being the formation of a PrP^{Sc} oligomer, which acts as a nucleus for the growth of larger oligomers (*5*, *16*).

The mature form of PrP^{C}, made up of residues 23−231, is anchored to the cell membrane via a glycosylphosphatidylinositol anchor (GPI anchor) at its C-terminus (*17*−*19*) and has two *N*-glycosylation sites (*20*−*22*) and one disulfide bridge. Three-dimensional NMR structures of the full-length and N-terminally truncated forms of recombinant murine PrP [*Mo*PrP (*23*−*26*)] and Syrian hamster PrP [*Sh*PrP (*27*−*29*)] have revealed that the whole N-terminal segment PrP(23−126) is flexibly disordered and that only the C-terminal part PrP(127−231) possesses a defined three-dimensional structure. For both species of PrP, this structurally well defined part consists of three α-helices and a small two-stranded antiparallel *β*-sheet. NMR structures of the C-terminal portion only of PrP, *Mo*PrP(121−231) (*23*, *24*) (PDB: 1AG2) and *Sh*Pr(P90−231) (*27*, *29*) (PDB: 1B10), showed the same general features in the full-length PrP NMR experiments (*25*, *28*). The three α-helices could be identified in all NMR structures very consistently, even though with slightly different length. On the other hand, the antiparallel *β*-sheet was not always as well defined (*27*, *28*) and has, therefore, been suggested to serve as a possible nucleation site for the conversion of PrP^{C} into PrP^{Sc} (*5*).

Molecular dynamics (MD) simulation has become a powerful tool for studying the structure and dynamics of biologically important molecules (*30*−*32*). From many studies it has become apparent that water−protein interactions are very important for structural and functional aspects of biopolymer chemistry, and although the simulated system may become very large, the use of explicit water with periodic boundary conditions is necessary to obtain accurate dynamical behavior. With increasing computer power, simulations of 1 *μ*s are already reported (*33*). Apart from explicit treatment of the solvent, the treatment of the electrostatic interaction forces is important for obtaining accurate simulations (*32*). Calculation of long-range electrostatic interactions is the most time-consuming part of MD simulations. The usual practice is to truncate these Coulombic

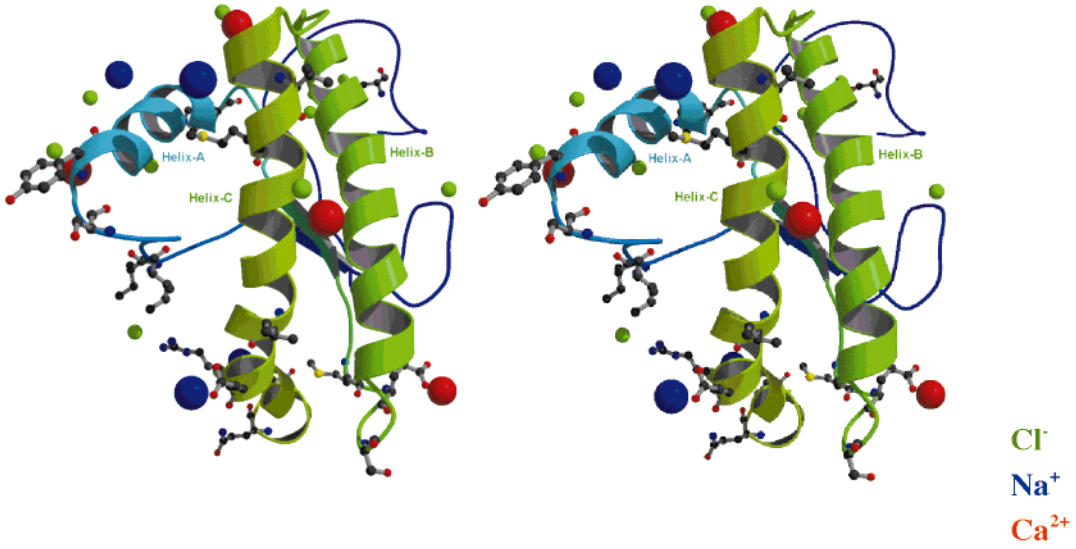

FIGURE 2: Stereoview of the *Hu*PrP−Ca starting model. Protein is shown in ribbons and counterions are shown as spheres (Cl^-, small green spheres; Na^+, blue spheres; Ca^{2+}, red spheres). Amino acids which have changed from the hamster PrP are shown in ball-and-stick representation. PrP coloring is graded from blue (N-terminal) to green (C-terminal). The picture was generated using MOLSCRIPT (*64*) and RASTER3D (*65*).

interactions, neglecting those beyond a defined cutoff distance. While the truncation discontinuity can be smoothed by applying switching or shift functions to the energies (*34*), nevertheless all these methods lead to errors in the calculation of Coloumbic forces acting on atoms (*35*, *36*). In particular, highly charged molecules such as nucleic acids tend to become unstable during MD simulations when truncation methods are applied (*37*). Adding salt ions to balance the charges and neutralize the system leads to increased stability of the model in various simulations (*38*−*41*). Similarly, increased stability could be achieved by increasing the size of the water box and with it the cutoff distance (*42*), but this dramatically increases the computational time.

Another method to overcome the problem of correct treatment of the electrostatic interactions without extraordinarily long computational time is using the particle mesh Ewald (PME) method. This method considers all electrostatic interactions over the complete system but requires no more than double the computational time (*43*, *44*). The algorithm employs interpolation of reciprocal-space Ewald sums from a grid and computation of convolutions using fast Fourier transformation. The PME method has been used in the simulation of highly charged molecules, such as DNA and RNA, with the result that stable structures could be obtained during simulations of up to 5 ns (*45*−*48*). Similarly, reduced backbone mobility is observed in protein systems which are less charged than polynucleosides (*32*, *46*). Additionally, the PME method has been shown to be a robust method insensitive to the size of the water box used in the simulation, as minimum solute-box edge distances of 5, 10, and 15 Å showed no significant differences in these MD simulations (*49*).

For application of the PME method a neutral system is required (*43*). One reported way to achieve this is to change the partial atomic charges of highly charged residues, like phosphates in DNA or RNA (*50*), such as to give a zero net charge for the whole model. A more realistic way to neutralize the system is to add salt ions to balance the charge. Counterions, like sodium and chloride, are placed near charged groups in regions with most favorable electrostatic potential for binding, using either geometric or energetic criteria or using procedures with a genetic algorithm (*51*). In addition, the concentration of these counterions was reported to influence the dynamical behavior of the simulated structure, as adding extra salt ions (in addition to the charge-balancing counterions) increased the stability of protein structures (*42*, *52*−*54*) even further.

To date, no three-dimensional structure for human PrP (*Hu*PrP) has been reported. Our main aims in this work were to build a homology model of *Hu*PrP and analyze its structural and dynamical behavior by MD simulations. The sequence similarity between mouse or hamster PrP and human PrP is quite high, with differences mostly in the C-terminal *structured* part (see Figures 1 and 2). The homology model of *Hu*PrP was made using the NMR structure of hamster PrP and included residues 90−230. Although the homology model included both the flexible (PrP90−126) and structured (PrP127−228) parts of PrP, the analysis was focused mainly on the structured part where most of the known disease-associated mutations are located. The first MD simulations of the homology model indicated a highly unstable structure. To find simulation parameters which result in a stable structure of *Hu*PrP, we analyzed the influence of different electrostatic interaction treatments and different ionic environments on the stability of the *Hu*PrP model. For comparison, a model of the *Sh*PrP NMR structure, *Sh*PrP(90−231), with the extended ionic environment was simulated using the two different treatments for the electrostatic interactions. Both PrP models, human and hamster, showed the same instability when the truncation method was used but showed stable structures when the correct treatment of the electrostatic interactions was used. The latter trajectories were analyzed to describe the dynamical and structural properties of PrP.

METHODS

All calculations were carried out using the AMBER 5 package (*55*, *56*) and the all-atom force field of Cornell et

Table 1: Summary of Simulation Conditions and Results for *Sh*PrP and *Hu*PrP

	*Sh*PrP		*Hu*PrP					
models	Na	Na	Cl	Na	Ca	Cl	Na	Ca
Cl^-, Na^+, Ca^{2+} ions	12, 9, 0	12, 9, 0	1, 0, 0	13, 12, 0	13, 4, 4	1, 0, 0	13, 12, 0	13, 4, 4
electrostatic	cutoff	PME	cutoff	cutoff	cutoff	PME	PME	PME
simulation time (ps)	720	1120	720	600	1500	720	720	1120
average temp[a,b] (K)								
PrP	316.5	299.3	310.2	316.5	316.5	299.4	299.7	299.2
water	361.7	298.5	342.0	362.4	341.2	298.5	298.5	298.4
RMSD[a,c] (Å)								
all (90−231)	6.2	5.0	6.0	4.9	8.7	3.3	3.9	4.4
N-terminus (90−125)	7.3	6.0	6.7	5.2	10.2	4.3	5.4	4.8
structured (126−227)	4.3	3.0	4.3	3.4	4.8	2.3	2.1	2.0
secondary structure[a] (%)								
α-helix	18.5	35.1	20.9	21.8	13.6	28.7	34.0	34.9
3_{10}-helix	8.1	7.5	13.1	10.7	19.8	10.7	9.7	10.7
β-strand	0.0	2.9	3.6	3.4	2.7	3.4	4.1	3.5
H-bonded turn	22.7	17.1	19.1	20.3	27.1	25.2	20.2	16.9
radius of gyration[a,d] (Å)	17.1	17.8	17.4	17.4	16.9	16.2	15.7	16.6
diffusion coef[e] (m^2/s)								
Cl^-, 2.05[f] × 10^{-9}	7.53	2.33	6.07	7.49	8.07	4.53	2.98	2.26
Na^+, 1.34[f] × 10^{-9}	4.78	1.54		4.12	5.98		1.16	1.92
Ca^{2+}, 0.80[f] × 10^{-9}					0.90			0.34

[a] Corresponding average values over the whole simulation. [b] 300 K was used as the simulation temperature for all models. [c] RMSD of backbone atoms: $[(1/N_A)\sum(r_i(t) - r_i(t_0))^2]^{1/2}$, with $r_i(t)$ coordinates of atom i at time t and N_A the number of atoms. [d] Radius of gyration: $[(1/N_A)\sum(r_i(t) - r_{CM}(t))^2]^{1/2}$, with r_{CM} coordinates of the center of mass. [e] Diffusion coefficient (D) obtained from mean square displacement of the salt ions using the Einstein relation $\langle|r(t) - r(t - \Delta t)|^2\rangle = 6D\Delta t$. [f] Experimental diffusion coefficient at 300 K.

al. (*57*). For the Na^+ and Ca^{2+} ions, the nonbonding interaction parameters were adapted from ion−water interaction potentials (*58*) leading to the following values: R^*_{Na} = 1.8762 Å, ϵ_{Na} = 0.0028347 kcal/mol, R^*_{Ca} = 1.3333 Å, and ϵ_{Ca} = 0.4597900 kcal/mol.

HuPrP Models. To build an homology model for *Hu*PrP, we used the NMR structure of *Sh*PrP [Brookhaven Protein Data Bank (PDB) entry 2PRP (*27*)]. The homology model was built with the program MODELLER Version 4 (*59*) using the sequence alignment shown in Figure 1 and default parameters. To refine the positions of the side chains, the resulting model was surrounded by a 79 × 78 × 79 Å TIP3 water box, minimized for 1500 steps and then subjected to a 60 ps long MD simulation starting at 600 K, cooling to 300 K within 5 ps, and then keeping the temperature at 300 K. During the simulation, the backbone of *Hu*PrP was restrained to its position after the minimization, and the restraint force was gradually reduced from 100 kcal/(molÅ^2) to 0 within 50 ps. The simulations were carried out using periodic boundary conditions and constant volume (NVT), 1 fs step size, and a temperature rescaling every 0.2 ps.

After initial refinement of the homology model the protonation states for the ionizable residues were set to their ionization state at pH 7 as calculated with the program TITRA (*60*). Thus, Glu and Asp were negatively charged and Lys and Arg positively charged. All the histidines (positions 96, 111, 140, 155, and 187) were protonated at the ϵ-position, based on an analysis by the program WHATCHECK (*61*). After setting the protonation state, the model had a total charge of +1 eu. To neutralize the system, salt ions were added to the model. As defined above, three different models for the salt ions were constructed (see Table 1):

(A) *Hu*PrP−Cl: In the first model, only one Cl^- ion was added (using LEAP in AMBER 5), corresponding to the minimum number of counterions necessary to neutralize the system. Considering an average volume of ∼185 000 Å^3 of the water box during the MD simulations, this would correspond to a solution concentration of ∼9 mM Cl^- ions.

(B) *Hu*PrP−Na: For the second model, the Cl^- and Na^+ ions were placed near each charged residue on the surface using the AMBER 5 program CION. This explores the electrostatic energy surface near charged residues to find positions with favorable counterion−protein interactions. A total of 13 Cl^- and 12 Na^+ ions were added, corresponding to solution concentrations of ∼116 mM Cl^- and ∼107 mM Na^+ ions.

(C) *Hu*PrP−Ca: The third model was generated by manually replacing each of the four pairs of close Na^+ ions in the *Hu*PrP−Na model by one Ca^{2+} ion. These pairs of Na^+ ions arose from two Asp or Glu side chains being close together on the surface of PrP. One Ca^{2+} ion was placed on the surface of helix A (see Figure 1 for secondary structure definitions) close to Asp144 and Asp147, one at turn C close to Asp167 and Glu168, one between turn D and helix C bridging Glu196 and Asp202, and the last one on the surface of helix C close to Glu207 and Glu211. The resulting model had 13 Cl^-, 4 Ca^{2+}, and 4 Na^+ ions, corresponding to solution concentrations of ∼117 mM Cl^- and ∼36 mM Na^+ and Ca^{2+} ions. Figure 2 shows this model as a stereoview.

All three different models were then immersed in a rectangular box of preequilibrated TIP3 water molecules of 66 × 63 × 58 Å size, resulting in systems with 5183, 5143, and 5147 water molecules for the *Hu*PrP−Cl, *Hu*PrP−Na, and *Hu*PrP−Ca models, respectively, and with total numbers of 17 730, 17 634, and 17 642 atoms.

ShPrP Model. The model for the NMR structure of *Sh*PrP-(90−231) was prepared in the same way as the models for *Hu*PrP. The protonation states for the ionizable residues were set to their ionization state at pH 7 as calculated with TITRA, resulting in negatively charged Glu and Asp residues and positively charged Lys and Arg residues and a net charge of +3.0 eu. Histidine residues 96, 111, 140, and 177 were protonated at the δ-position and His187 at the ϵ-position, as

calculated by WHATCHECK. To neutralize the model, the positions of Na^+ and Cl^- ions were calculated by CION, resulting in a model with 9 Na^+ ions and 12 Cl^- ions. The model was immersed in a rectangular box of preequilibrated TIP3 water molecules of 67 × 63 × 57 Å size, resulting in a model with 5104 water molecules and 17 540 atoms (*Sh*PrP−Na in Table 1).

MD Simulation. All simulations were performed using the SANDER module in the AMBER package. Newton's equations of motion were integrated with a step size of 1 fs, with lengths of all bonds involving hydrogen atoms constrained using the SHAKE algorithm and a relative tolerance of 5×10^{-6} Å. A pair list to calculate nonbonded interactions was generated every 50 simulation steps. The temperature of the system was controlled to be 300 K using two independent Berendsen thermostats (*62*), one for the solute and one for the solvent, and with coupling times $\tau_{solute} = 0.5$ ps and $\tau_{solvent} = 0.75$ ps. Overall translational and rotational motion of the system was removed every 100 time steps. The electrostatic interactions were calculated by two different methods, one by truncating the interaction (cutoff) and one by calculation of the long-range interactions using the particle mesh Ewald method (PME) implemented in SANDER (*43*). For the cutoff method, a cutoff distance of 8 Å was used. For the PME method, a grid size of 64 × 64 × 64 as used, equal to a grid spacing of ∼1 Å or less.

To equilibrate the system, all models were first minimized (1500 steps) and then subjected to a 30 ps constant pressure (NPT) simulation, starting from 600 K with atom velocity assignment according to a Maxwell distribution and cooling to 300 K within 5 ps. Temperature and pressure couplings were gradually reduced over the 30 ps period, and the update frequency of the nonbonded atom list decreased from once every 15 fs to once every 50 fs. The density equilibrated in all simulations to a value ∼1.0 g/mL, and the box size shrank to approximately to 61 × 58 × 53 Å for all models. An additional 20 ps constant volume simulation (NVT) with model-specific simulation parameters (cutoff or PME) was performed before the trajectory was used for analysis. The analyzed trajectories were taken from constant volume simulations (NTV) which had periods of 20 ps constant pressure simulations (NPT) every 80 ps of NTV simulation. These NPT periods were included to compensate for any possible volume change due to major conformational changes. However, no major volume change occurred during these NPT simulation periods.

The calculations were carried out on SGI Power-Challenge (SGI-PC) and on Fujitsu VPP300 (VPP) supercomputers. On the VPP platform an optimized version of the SANDER module was used, which improved the simulation time from 0.88 s/step to 0.62 s/step for a cutoff simulation with 17 540 atoms (5104 water molecules) and from 2.93 s/step to 1.37 s/step for the corresponding PME simulation. The corresponding times on the SGI-PC (R10000, 194 MHz) are 1.20 s/step (cutoff) and 2.71 s/step (PME).

Trajectory Analysis. NMR experiments on *Sh*PrP revealed a highly flexible N-terminal part with only the C-terminal part having a defined secondary structure. Therefore, all the root-mean-square deviation (RMSD) analysis of the structure has been calculated not only for the complete model (PrP90−230) but also for the *flexible* part (PrP90−126) and the *structured* part (PrP127−227) separately. Analysis of molecular trajectories was done with the program CARNAL in AMBER 5, including structural alignment and calculation of the RMSD of the structure, radius of gyration, translational diffusion coefficient, and radial distribution functions for the ions. Analysis of the secondary structure and pK_a values were done with the DSSP (*63*) and the TITRA (*60*) program. Salt bridges were defined by the distance between the positively and negatively charged heavy atoms. For Arg residues, all three nitrogen atoms of the side chain, N^{ϵ}, $N^{\eta 1}$, $N^{\eta 1}$, were used. A salt bridge was deemed present if the distance between the two heavy atoms less the corresponding van der Waals radii was smaller than 1.5 Å. For model manipulation and visual analysis, INSIGHTII (MSI) was used. The pictures were generated using MOLSCRIPT (*64*), RASTER3D (*65*), MOLMOL (*66*), and POVRAY (http://www.povray.org).

RESULTS

HuPrP Homology Model. The differences between the *Sh*PrP and the *Hu*PrP sequences are mainly in the C-terminal part of the protein, the region which shows defined secondary structure in the NMR structures of *Sh*PrP and *Mo*PrP (see Figures 1 and 2). These differences involve three changes (138, 139, 143) in turn A (the turn before the first α-helix, helix A), two changes (145, 155) in helix A, three changes (166, 168, 170) in turn C (the turn between the second β-strand, strand B, and the second α-helix, helix B), and five changes (203, 205, 215, 219, 220) in the third α-helix, helix C. The differences involving the *flexible* part are one (97) in the N-terminal region and three (227, insertion before 228, 229) at the C-terminus, which in the *Hu*PrP homology model has been defined as an elongation of helix C. Although most of the changes occur in the *structured* part of the protein, most of these involve residues which are well exposed on the surface of ShPrP (see Figure 2), and consequently, their replacement in the *Hu*PrP model does not require major structural adjustments of the neighboring residues. Only 4 of the 17 changes involve residues whose side chains are buried: Trp145→Tyr (helix A), Gln168→Glu (turn C), and Ile203→Val and Ile205→Met (both helix C). But apart from Ile205→Met, all changes are to residues with smaller side chains. Additionally, most of the changes are to residues with similar properties (polar, hydrophobic), so that the overall properties of the protein are not changed much. Most of the changes involving charged side chains are on helix C or at the C-terminus and are well exposed.

To refine the conformations of the side chains, a 60 ps long MD simulation was carried out on the homology model with the backbone conformation restrained to its energy-minimized starting position, resulting in a RMS deviation from the NMR structure of 2.1 Å. Despite the high RMSD, the secondary structure elements in the homology model are the same as in the NMR structure, but with slightly different length: NMR structure with 37.3% α-helical, 2.1% 3_{10}-helical, 2.8% in β-strand, and 16.9% in H-bonded turns; *Hu*PrP model with 31.9% α-helical, 7.8% 3_{10}-helical, 4.3% in β-strand, and 15.6% in H-bonded turns. The only significant difference between the *Sh*PrP NMR structure and the *Hu*PrP model is in the number of salt bridges found. In addition to the salt bridge Asp178↔Arg164 between helix

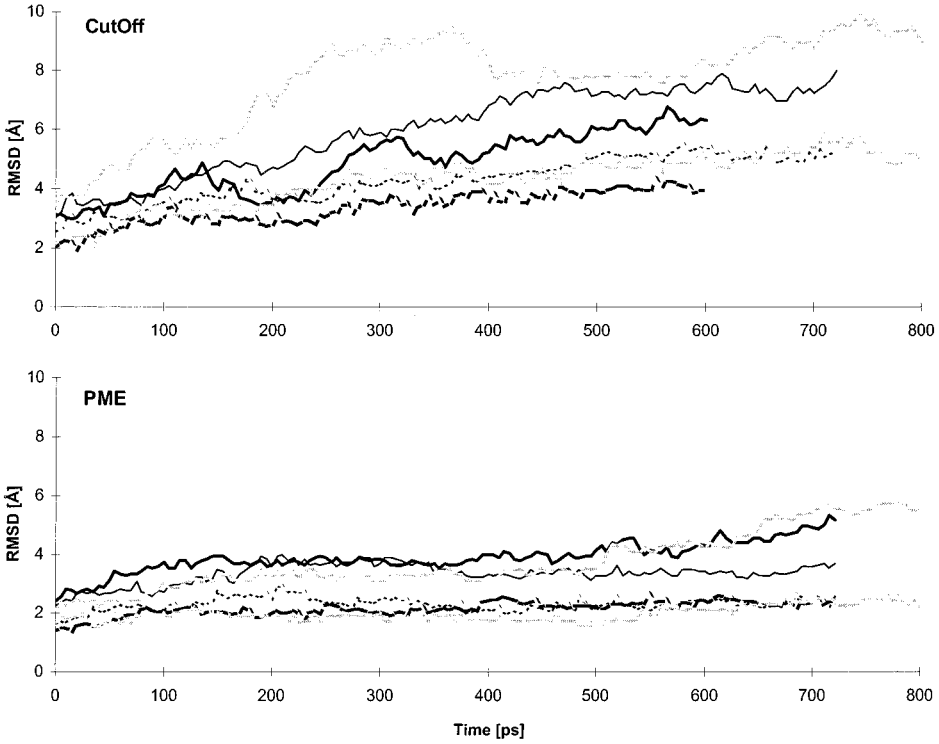

FIGURE 3: Root-mean-square deviation (RMSD) of the backbone atom positions, from their starting positions as a function of time, for simulations of the *Hu*PrP model with different treatments of the electrostatic interactions. CutOff: using the cutoff method with a value of 8 Å. PME: using the particle mesh Ewald summation method. The RMSD is shown in both cases for all different salt ion models, Cl (thin line), Na (thick line), and Ca (gray line), and for the whole model PrP(90−230) as a solid line and for the *structured* part of the protein PrP(127−227) as a dotted line.

B and strand B, which is present also in the NMR structure of *Sh*PrP, two more salt bridges were found in the *Hu*PrP model: Glu146↔Arg208 between helix A and helix C and Glu196↔Arg156 between turn D and the end of the helix A, both resulting from small conformational changes in the corresponding regions. By comparison, the NMR structure of *Mo*PrP (*26*) shows two of the three salt bridges, Asp178↔Arg164 and Glu196↔Arg156. The refined structure was then used as the starting conformation for all the MD simulations.

MD Simulations: *Cutoff Method*. To analyze the structural and dynamical behavior of the *Hu*PrP model, several series of MD simulations were carried out. In the first series, the time-saving cutoff method was used to calculate the electrostatic interactions. The first simulation of this series was performed with a model in which *Hu*PrP was neutralized with just one Cl^- ion (*Hu*PrP−Cl). As can be seen in Figure 3, this simulation showed high instability of the protein model, resulting in a very large RMS deviation of the backbone atoms of up to 10.0 Å from their starting positions. Even considering only the *structured* part of PrP, a RMSD of more than 5 Å is calculated. Analysis of the secondary structure by the DSSP method, shown graphically for the first 700 ps in Figure 4 (*Hu*PrP−Cl−cutoff) and as the average structure content in Table 1, gives the same picture of an unstable trajectory for this simulation. Helix A and, especially, helix C nearly disappear, and the α-helical structure content decreases to 20.9%. Most of the α-helical structure shifts to a 3_{10}-helical form, increasing the corresponding content to 13.1%. The β-strand content, on the other hand, remains at 3.6%, near its starting value (see Table 1).

Explicit salt ions have been reported to increase the stability of proteins in MD simulations using the cutoff method (*42*, *52*). Hence, a simulation was carried out on the *Hu*PrP model with 13 Cl^- and 12 Na^+ ions (*Hu*PrP−Na), corresponding to a solution concentration of ∼110 mM NaCl. Even though the protein displays a slightly higher stability than in the previous *Hu*PrP−Cl simulation, the RMSD of the backbone atoms for just the *structured* part of the protein reaches a value of 4 Å after 500 ps. Secondary structure analysis reveals the same decrease in α-helical content as in the *Hu*PrP−Cl simulation (21.8% α-helical structure content), with helix A slightly more stable but with helix C nearly disappearing again.

The initial conformation for these simulations has eight Asp/Glu side chains forming 4 pairs of Asp/Glu residues on the surface of the protein. Addition of Na^+ counterions near their negatively charged side chains resulted in four Na^+ pairs at distances less than 4 Å. During the *Hu*PrP−Na simulation most of these Na^+ ions diffuse into the solvent, leaving pairs of negatively charged side chains unbalanced. As this might contribute to the instability of the protein, these Na^+ ion pairs were replaced by single Ca^{2+} ions to bridge between the two Asp/Glu side chains. These Ca^{2+}-mediated salt bridges involve Asp144↔Asp147 on the surface of helix A, Asp167↔Glu168 close to turn C, Glu196↔Asp202 between turn D and helix C, and Glu207↔Glu211 on the surface of helix C. However, simulation of this Ca^{2+} ion model (*Hu*PrP−Ca) shows that although the Ca^{2+} ions remain within a salt-bridge distance to the Asp/Glu side chains throughout the simulation, the protein has an even lower stability than in the previous *Hu*PrP−Cl and *Hu*PrP−Na

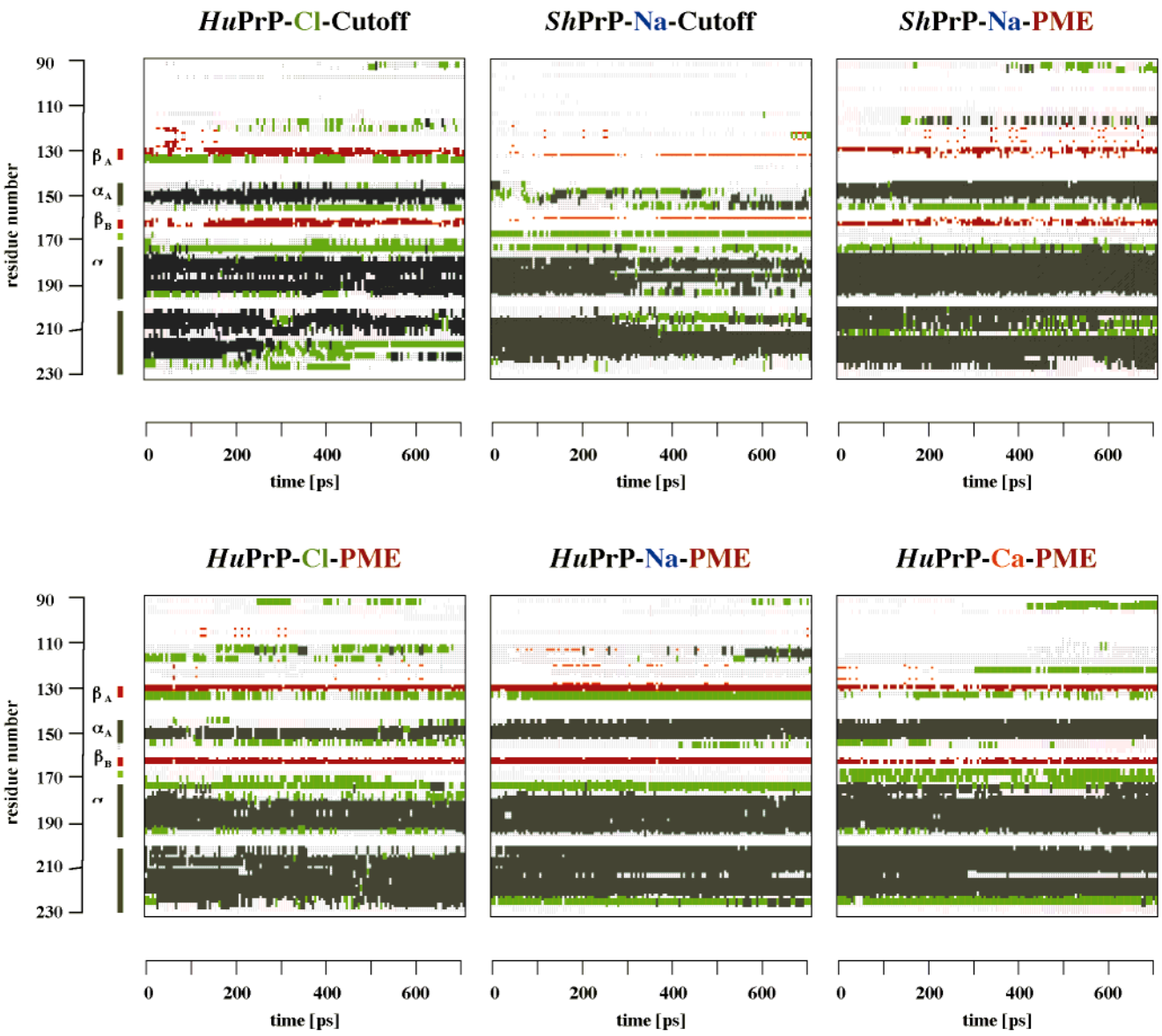

FIGURE 4: Secondary structure as a function of simulation time for different models. The α-helix is shown in dark green boxes, the 3_{10} helix in light green boxes, the *β*-strand in red boxes, and the H-bond turn as gray dots. The secondary structure bar at the side is from *Sh*PrP(90−231) (*29*).

simulations. The RMSD of backbone atoms of the *structured* part (see Table 1 and Figure 3) exceeds 5 Å after 500 ps, and the α-helical content decreases to only 11.3%. A notable feature of all three simulations (Cl, Na, and Ca) is that the content of the *β*-strand remains at its initial value of ∼3%. It seems that the instability affects mainly α-helical structures.

MD Simulations: *PME Method*. Simulations of DNA and RNA highlighted the importance of the correct treatment of long-range electrostatic interactions for stability of the DNA/RNA structure (*45*, *48*, *49*). In SANDER, the treatment of long-range electrostatic interactions is implemented by the particle mesh Ewald (PME) method (*43*). Simulations of all three counterion models of *Hu*PrP using the PME method instead of the cutoff method were carried out. All these simulations showed high stability of the PrP model, with RMSDs of the *structured* backbone atoms between 2.0 and 2.3 Å. Secondary structure analysis, shown graphically in Figure 4 for all three PME simulations, shows much more stable helices A and C than in the cutoff simulations. The content of α-helical structure remains within the range 28.7−34.9%, close to its starting value of 31.9%, as does the *β*-strand content at 3.4−3.5%.

To see if the sensitivity of the model with respect to the treatment of the electrostatic interactions is dependent on the *Hu*PrP structure being an homology model, simulations of the *Sh*PrP NMR structure (*Sh*PrP−Na, with 12 Cl^- and 9 Na^+ ions) were carried out using both the cutoff and PME methods. RMSD values (Table 1) and secondary structure analysis (Figure 3) show similar behavior as in case of the *Hu*PrP model. Simulation with the cutoff method shows a RMSD of the *structured* backbone atoms of 4.3 Å, a decrease of the α-helical content to 18.5%, and a complete decay of the *β*-structure. On the other hand, simulation with the PME method gives a more stable trajectory, with a RMSD of 3.0 Å, slightly higher than the corresponding value for the *Hu*PrP model, but with similar secondary structure content, 35.1% for α-helical and 2.9% for *β*-strand.

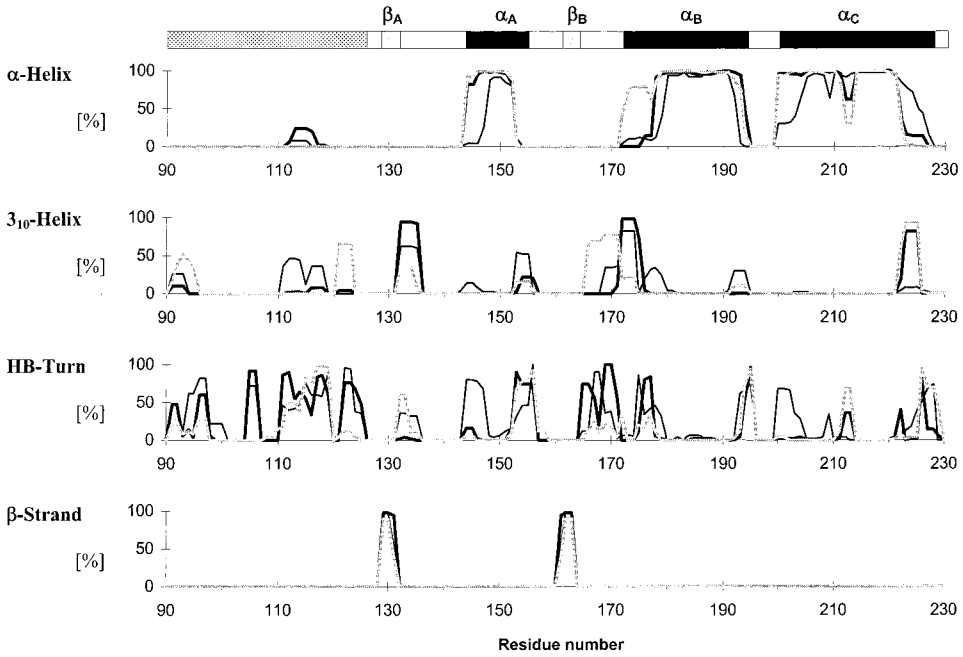

FIGURE 5: Secondary structure per residue averaged over the complete simulations of *Hu*PrP−PME. The per residue percentage of secondary structure defined by the DSSP method is shown for the different counterion models: Cl (thin line), Na (thick line), and Ca (gray line). The secondary structure bar at the top is from *Sh*PrP(90−231) (*29*) (solid for α-helices, shaded for *β*-sheets, and stippled for the flexible region).

Further analysis of all the cutoff simulations indicated that these systems showed an increased temperature. Although the bath temperature was set to 300 K, the average temperature of the system increased to 310−316 K for the protein and 341−361 K for the solvent (see Table 1). In contrast, simulations of all the PrP models using the PME method gave a more stable temperature, with the average temperatures for protein and solvent remaining close to the bath temperature of 300 K (see Table 1). Short test simulations of about 200 ps (data not shown) showed that, in the case of a cutoff simulation, using a tighter temperature coupling could lower the temperature of the system but led to structures as unstable as in the initial cutoff simulations. Similar short simulations with the PME method at a higher temperature (320 K), however, did not show a less stable structure than at 300 K. It has been suggested that the PME method introduces artificial periodicity into the system (*67*), thus increasing the stability of the most compact conformation of DNA or proteins (*68*). For simulations with the *Hu*PrP models, the radii of gyration, shown in Table 1 as average values, are slightly *reduced*, by 0.3−1.7 Å, if the PME method is used. On the other hand, for simulations with the *Sh*PrP structure, the radius of gyration is *increased* from 17.1 to 17.8 Å if the PME method is used. The corresponding average value for the *Sh*PrP NMR structure (*27*) is 17.2 Å.

Secondary Structure of HuPrP Models. The secondary structure analysis, shown graphically in Figure 4 and as percentage occurrence averaged over the simulation time as a function of residue number in Figure 5, reveals that, while the *β*-strand conformations have a similar extent in all three *Hu*PrP models using the PME method, the α-helical structures differ significantly. Table 2 shows the lengths of secondary structure elements in the NMR structures of *Sh*PrP(90−231) (*29*) and *Mo*PrP(121−231) (*26*) and in the simulations of the *Sh*PrP and *Hu*PrP models. The *Hu*PrP−Cl model, with only one Cl^- ion, shows all the α-helices to be shortened, mostly due to shift to 3_{10}-helical conformation. The *Hu*PrP−Na model shows more stable α-helical structure. In comparison with the refined NMR structure of *Sh*PrP-(90−231), helix A is shorter by two residues at its C-terminal end and helix B is shorter by six residues at its N-terminal end. Helix C not only is shortened by six residues at its C-terminal end but also has two residues (Gln212 and Met213) which are ∼40% of the time in H-bonded turn conformation, thus tending to split helix C. The simulation with the *Hu*PrP−Ca model shows helix B only one residue shorter than the NMR structure and helix A with the same length as in the *Hu*PrP−Na model, but with an even more developed split of helix C (70% of the simulation time). The refined NMR structure of *Mo*PrP(121−231) also shows a split of helix C, but the split occurs at 220−221 and includes a sharper bend than in the *Hu*PrP models. The *β*-strands in all structures, both NMR and MD models, are of similar length, although in the MD simulations they have a tendency to be even shorter, more typical of the NMR structure of *Sh*PrP than of *Mo*PrP. Even though α-helical structures are different between the NMR structures and the homology model, the overall structures are similar and differ only in the flexible regions of the PrP, including turns C, B, and D, as shown in Figure 6.

Table 2: Positions of Secondary Structure Elements for the *Mo*PrP(121−231) (*26*) and *Sh*PrP(90−231) (*29*) NMR Structures and for the MD Simulation Structures Using the PME Method

	*Mo*PrP	*Sh*PrP		*Hu*PrP		
	NMR (*26*)	NMR (*29*)	Na PME	Cl PME	Na PME	Ca PME
β_A	128−131	129−131	129−130	129−131	129−131	129−130
β_B	161−164	161−163	162−163	161−163	161−163	162−163
α_A	144−154	144−154	144−151	148−152	144−152	144−152
α_B	175−193	172−193	176−194	180−192	178−193	173−193
α_C	200−219	200−227	200−209	204−225	200−221	200−210
α_{C2}	222−226		213−227			214−221

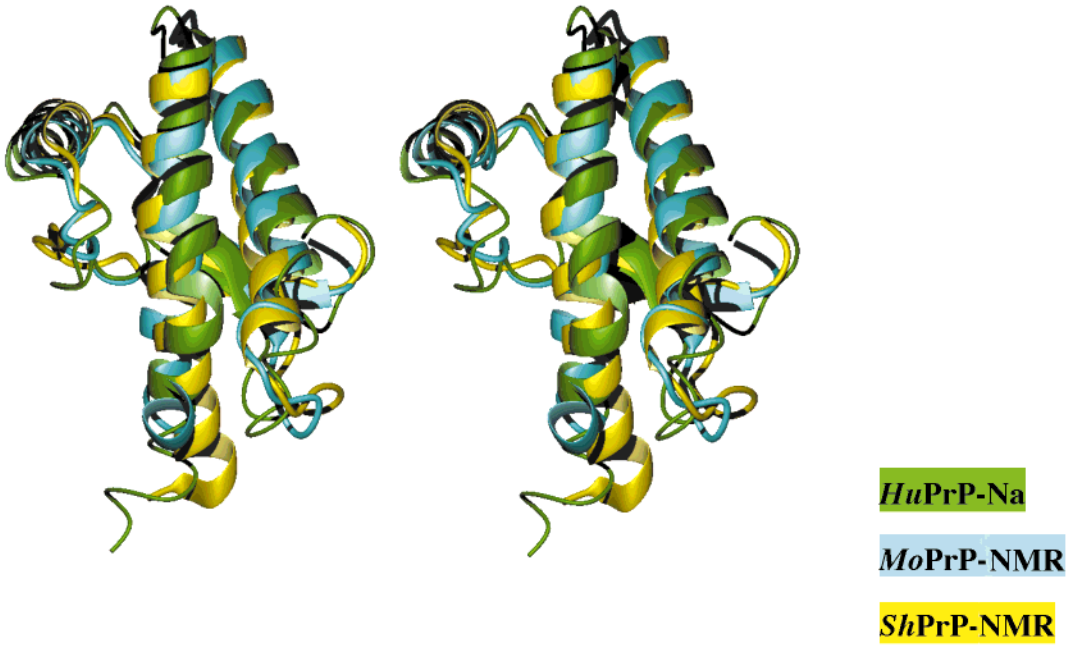

FIGURE 6: Stereoview of the averaged structure of the *Hu*PrP−PME−Na simulation in green, superimposed with the NMR structures of *Mo*PrP (*26*) in cyan and *Sh*PrP (*29*) in yellow. All structures are shown with their corresponding secondary structures.

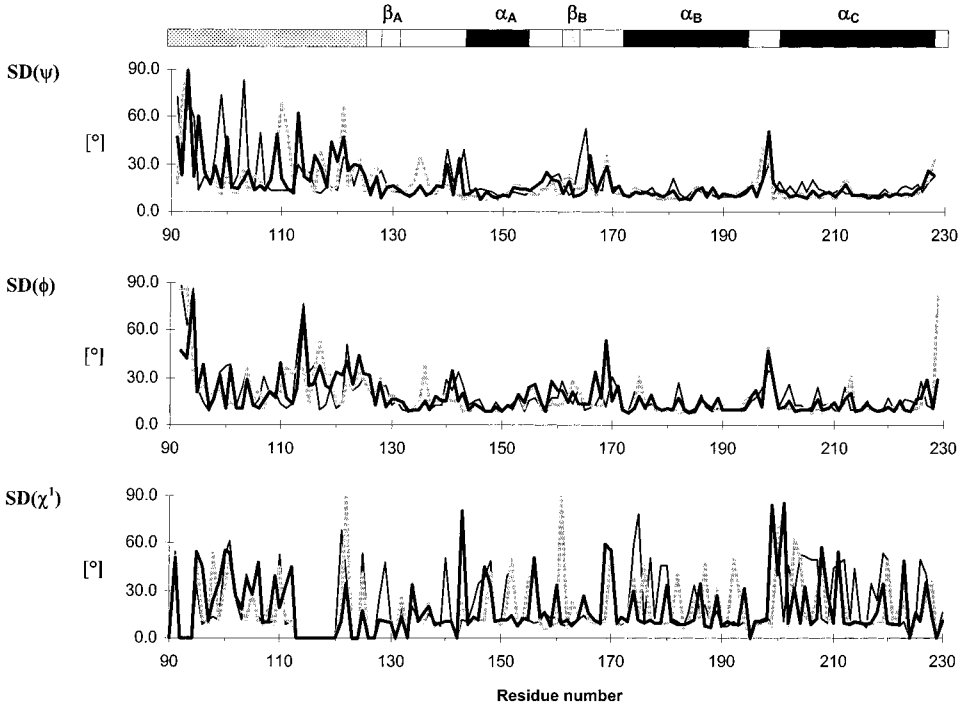

FIGURE 7: Standard deviations (SD) of the backbone torsion angles, ϕ and ψ, and for the first side chain torsion angle, χ^1, (except for Gly and Ala residues), from the simulations of *Hu*PrP−PME. The SDs are shown for all counterion models: Cl (thin line), Na (thick line), and Ca (gray line). The secondary structure bar at the top is from *Sh*PrP(90−231) (*29*) (solid for α-helices, shaded for β-sheets, and stippled for the flexible region).

Flexibility of HuPrP Models. The flexibility of the protein backbone was analyzed by calculating the standard deviations (SD) for the two backbone torsion angles, ψ and ϕ, as shown in Figure 7 for the *Hu*PrP models. The differences in flexibility between the different salt ion models of *Hu*PrP using the PME method are less pronounced than indicated by the secondary structure analysis. The *Hu*PrP−Cl model shows only slightly increased flexibility in the backbone torsion angles for the whole *structured* part, PrP(127−227). All ionic models show low flexibility for most of the structured part, with SDs for ψ and ϕ less than 15°. The region around Tyr169 in turn C, and around Phe198 in turn D, shows higher backbone flexibility, with SD values between 25° and 60°. Another flexible region within the structured part can be seen between Ile138 and Ser143 in turn A just before helix A. The region in turn B, between helix A and strand B, also shows slightly elevated SD values. Figure 7 also clearly identifies the N-terminal part, *Hu*PrP-(90−126), as highly flexible, with SD values greater than 30°. However, within this region, a small patch (from Ser97

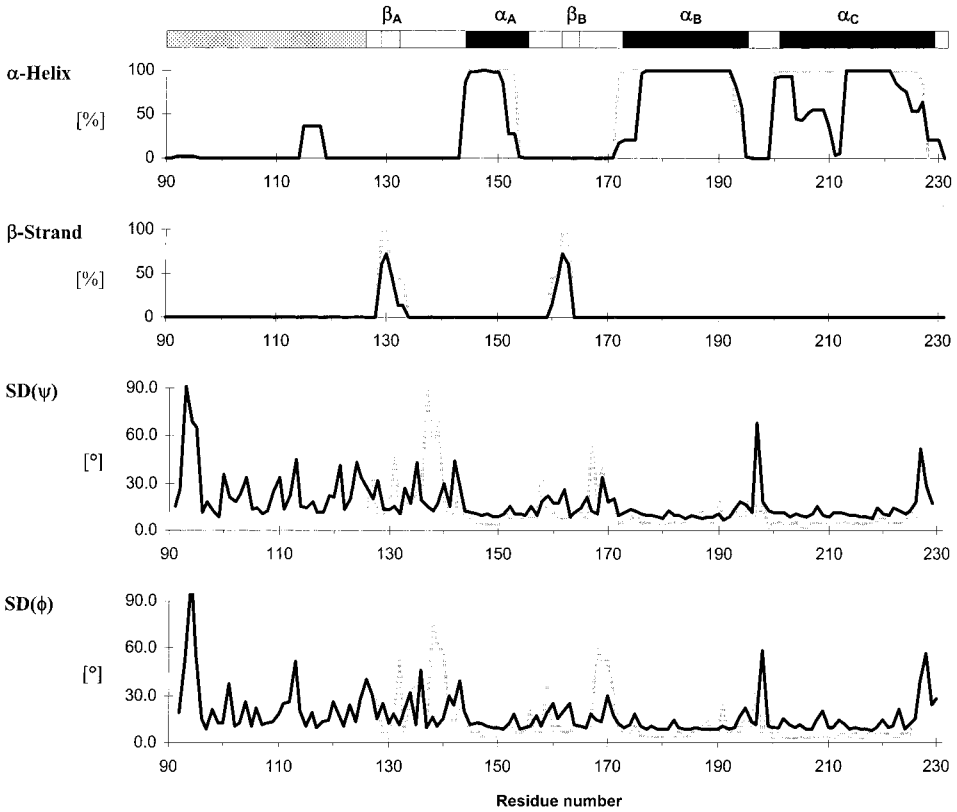

FIGURE 8: Secondary structure per residue averaged over the complete simulation and standard deviation (SD) of the backbone torsion angles, ϕ and ψ, for the *Sh*PrP−PME−Na (thick line) simulation and for the NMR structure (gray line), calculated from the 25 NMR conformations in PDB 1B10. The secondary structure bar at the top is from *Sh*PrP(90−231) (*29*) (solid for α-helices, shaded for β-sheets, and stippled for the flexible region).

to Asn108) can be identified with somewhat reduced flexibility. This does not show any secondary structure but includes two proline residues which restrict the flexibility. A short region (113−116) of α-helical conformation formed for 25% of the simulation is apparent only in the *Hu*PrP−Na model. Analysis of the first side chain torsion angle, χ^1, also shown in Figure 7, shows no clear pattern either among the different ionic models or between the *structured* and *flexible* parts.

ShPrP Model. The *Sh*PrP model starting from the NMR structure showed the same sensitivity to the correct treatment of the electrostatic interactions (see Figure 4). Although the simulation with the PME method showed a more stable trajectory, detailed analysis of the secondary structure reveals a less stable secondary structure than for the *Hu*PrP model. As shown in Figures 4 and 8, helix C splits totally and forms two separate α-helical structures (see Table 2), with 3_{10}-helical conformation in between. Helices A and B show similar lengths as in the *Hu*PrP model, as do the β-strands. The SD analysis of the backbone torsion angles indicates similar flexibility in turns A−D as in the *Hu*PrP model. It also shows higher flexibility of the region just after strand A. The flexible N-terminal part shows high flexibility with intermittent appearance of α-helical structure in the region 115−118 for *Sh*PrP−Na. The 25 NMR structures of *Sh*PrP show flexibility in the turn regions as for the simulations, but with different magnitudes. Turns A and C show greater flexibility in the NMR structure, whereas turn D shows greater flexibility in the simulations.

Salt Ions in HuPrP Model. In contrast to reports on other systems (*42*), salt ions are not able to generate more stable PrP structures in simulations where the cutoff method is used. If the PME method is used for the electrostatic interactions, the salt ions seem to have a stabilizing effect on the trajectory of *Hu*PrP. As also reported for the simulation of a βARK1 PH domain (*54*), salt ions initially placed on the surface of the protein move into the solvent. Cl^- ions, in particular, show only minor interactions with the protein, tending to stay in the solvent. The diffusion coefficients (D) for Cl^- ions in the *Hu*PrP−Na and *Hu*PrP−Ca models are higher than the experimental value (see Table 2). In the case of *Hu*PrP−Cl, the value for D_{Cl} is derived from only one Cl^- ion and is, therefore, not reliable. The Na^+ ions in the *Hu*PrP−Na model show some interaction with the protein, resulting in a diffusion coefficient lower than the experimental value. In case of the *Hu*PrP−Ca simulation, some Na^+ ions are replaced by Ca^{2+} ions, resulting in increased D_{Na} and decreased D_{Ca} values, compared with their experimental values. The Ca^{2+} ions are actually not moving into the solvent at all. They remain close to their starting positions, making salt bridges between two Asp/Glu side chains throughout the whole simulation time but rarely exceeding a coordination number of 2 with the protein. As Ca^{2+} ions usually have a coordination number between 4 and 7 in Ca-binding proteins (*69*), the Ca^{2+} sites in the *Hu*PrP model cannot be considered as real Ca-binding sites. MD simulations showed that divalent cations such as Mg^{2+} influence the structure of DNA differently than monovalent cations such as Na^+ (*70, 71*), leading to different bending of the DNA structure. However, it appears that Ca^{2+} ions do not influence the structural behavior of the *Hu*PrP model differently from Na^+ ions. The sites where Ca^{2+} ions are

Table 3: Salt Bridges from Simulations of *Sh*PrP and *Hu*PrP, Shown as Percentage Occupancy during the Whole Simulation[a]

salt bridges negative↔positive	*Sh*PrP Na PME	*Sh*PrP NMR[b]	*Hu*PrP Cl PME	*Hu*PrP Na PME	*Hu*PrP Ca PME
Asp144 (α_A)↔His140 (τ_A)	8.9		38.4	23.0	
Asp144 (α_A)↔Arg148 (α_A)	83.3		5.3	23.9	38.7
Asp144 (α_A)↔Arg208 (α_C)	96.0				
Glu146 (α_A)↔Lys204 (α_C)		52.0	8.6		
Glu146 (α_A)↔Arg208 (α_C)		16.0	100.0	100.0	100.0
Asp147 (α_A)↔Arg151 (α_A)	38.4	76.0	99.3	11.9	15.5
Asp147 (α_A)↔His140 (τ_A)	74.5	52.0	40.5	37.7	92.9
Asp178 (α_B)↔Arg164 (τ_C)	99.9	12.0	73.4	97.4	96.7
Glu196 (τ_D)↔Arg156 (α_A)	98.0	20.0	96.1	99.4	48.0
Asp202 (α_C)↔Arg156 (α_A)			74.9		1.3
Glu211 (α_C)↔His177 (α_B)	3.3	16.0	0.1	5.6	28.3

[a] The secondary structure elements, corresponding to the NMR structure of *Sh*PrP, are shown in parentheses. Underlined residues are residues for which mutation is known to associated with CJD, GSS, or FFI in humans. [b] Calculated from the 25 conformations in PDB 1B10 (*29*).

located throughout the simulation are usually occupied by Na^+ ions in the *Hu*PrP−Na simulation. One of these sites with a strong ion−protein interaction is at Glu207 and Glu211, which is close to the site where in both ionic models, *Hu*PrP−Na and *Hu*PrP−Ca, the split in helix C occurs. The other strong interaction sites, Asp144↔Asp147, Asp167↔Glu168, and Glu196↔Asp202, do not seem to have such an influence on the structure of *Hu*PrP.

Salt Bridges. As salt bridges are suggested to increase the stability of proteins, a detailed analysis has been made for the simulations. This analysis includes also histidine residues, for which the pK_a value can be increased by proximity to negatively charged groups. At pH 7 or lower, such histidines are able to be protonated and, thus, are able to participate in salt bridges. The simulation models were generated in a protonation state corresponding to a pH value of 7. Thus, in the simulations, all the histidine residues are in the neutral unprotonated form, but analysis of the pK_a values during the simulation (with TITRA) indicates that His140 and His177 have increased pK_a values from 6.5 to 7.4. So, these histidines would sometimes during the simulations be more likely to be protonated.

Some highly occupied salt bridges were identified by analysis of the simulations (see Table 3). The most occupied salt bridge is that between Glu146 and Arg208, which is occupied 100% in all simulations of the *Hu*PrP model and 96% for the *Sh*PrP model. Not only is this a bridge between two sequence-distant residues, bridging helix A to helix C, but it also involves a residue, Arg208, for which a mutation is known to be associated with CJD in humans (*3*). Another dominant salt bridge could be identified between turn B and the turn D region, Arg156↔Glu196, occupied 48−99% in all simulations. A third salt bridge which might contribute to the stabilization of PrP was found between Arg164 and Asp178, linking the end of strand B and helix B and occupied 74−99% of the time. Mutation of Asp178 to Asn is known to cause CJD or FFI in humans, depending on the polymorphism at position 129 (*3*). Another salt bridge involving a residue (Asp202) for which mutation is known to be associated with GSS in humans (*13*) is between Asp202 in helix C and Arg156 in turn B. This salt bridge can be detected only in the simulation with the *Hu*PrP−Cl model, with an occupancy of 75%. The only potential salt bridges involving a possible protonated histidine residue are between His140 and Asp144 or Asp147. In the simulation with the *Hu*PrP−Ca model, only the salt bridge with Asp147 is detectable, bridging turn A and helix A. The remaining salt bridges found in the analysis are less occupied and involve mostly neighboring residues (e.g., ±4 in an α-helical structure). They are, therefore, not contributing to the stability of PrP. The differences between the salt ion models with respect to the salt bridges are not easy to generalize. Sometimes reduced occupancy of a salt bridge can be explained by a counterion blocking one of the charged residues, but it is not generally the case.

Hydrogen Bond Network. Analysis of the H-bond networks, shown in Table 4 for hydrogen bonds involving side chains and occurring for more than 30% of the simulation time in one of the models, reveals that some of the dominant H-bonds (occupancy above 90% in at least one of the models) involve neighboring residues in α-helical structures or at their end (marked in Table 4 with α±4), such as the H-bond between Thr183 O^γ↔Cys197 O in helix B, occupied 100% in all *Hu*PrP models, or Ser143 N↔Glu146 O^ϵ in helix A. All these α±4 H-bonds are highly occupied and involve one backbone atom. The remaining highly occupied H-bonds can be classified into three different categories of interactions: one between the β-strand region and helix B (Tyr162 N↔Thr183 O^γ and Arg164 N^η↔Asp178.O^δ) marked in Table 4 with $\beta-\alpha_{BC}$; the second between the region of turn A, helix A, and turn B, and helix C and turn D ($\alpha_A-\alpha_C$: Tyr149 O^η↔Asp202.O^δ and Tyr157 O^η↔Asp202 O^δ); and the last within the region of turn A, helix A, and turn B (α_A: Arg136 N^η↔Asn159 O^δ and Tyr150 O). Some of these H-bonds involve residues for which mutation is known to be associated with disease in humans, but some of these substitutions are to residues which are also able to make H-bonds (Asp202→Asn, Asn171→Ser, His187→Arg, and Arg208→His). Other known mutations such as Gln212→Pro would affect the secondary structure more than the H-bond network. Thr183 is the only residue in the H-bond network shown in Table 4 for which mutation would lead to a residue unable to contribute to an H-bond. This would affect an interaction between strand B and helix B and an interaction within helix B.

DISCUSSION

As most residue changes are on exposed areas of the protein surface, the structure of the homology model of human PrP (*Hu*PrP) is similar to the NMR structure of *Sh*PrP. The MD simulations showed similar dynamics behavior—stability of secondary structure and flexibility of N-terminal parts and turns—for *Sh*PrP and *Hu*PrP. In addition, both showed similar high sensitivity to correct treatment of the electrostatic interactions. In both cases, inclusion of all long-range electrostatic interactions in the simulation, using the PME method, was necessary to generate stable trajectories and structures for PrP. This sensitivity of the PrP model to the correct treatment of the electrostatic interactions may arise from the large number of charged or potentially charged residues on the surface of the protein. The NMR structure of *Sh*PrP(90−231) has six Lys, eight Arg, six His, six Glu, and three Asp on the surface. For *Hu*PrP(90−230), the number of exposed Glu residues is increased by two,

Table 4: Hydrogen Bonds Involving Side Chains and Occurring More than 40% of the Simulation Time in One of the *Sh*PrP and *Hu*PrP Models, Shown as Percentage Occupancy during the Whole Simulation[a]

H-bond donor↔acceptor		% H-bond occupancy				
		ShPrP		HuPrP		
		Na PME	NMR[b]	Cl PME	Na PME	Ca PME
Met109 N↔Thr107 O^{γ}		65		47	29	29
Gly123 N↔Tyr128 O^{η}		83		5	67	18
Arg136 N^{η}↔Tyr150 O (α_A)	α_A			99	99	89
Arg136 N^{η}↔Met154 O (α_A)	α_A	90	4		4	2
Arg136 N^{η}↔Asn159 O^{δ} (τ_B)	α_A		4	95	79	98
Ser143 N (τ_A)↔Glu146 O^{ϵ} (α_A)	$\alpha\pm4$	13	80		89	91
Tyr149 O^{η} (α_A)↔Asp202 O^{δ} (α_C)	$\alpha_A-\alpha_C$	81	20	66	51	1
Asn153 N^{δ} (α_A)↔Tyr149 O (α_A)	$\alpha\pm4$	90	96	99	99	94
Arg156 N^{ϵ} (α_A)↔Glu196 O^{ϵ} (τ_D)	$\alpha_A-\alpha_C$	94	4		77	14
Arg156 N^{ϵ} (α_A)↔Asp202 O^{δ} (α_C)	$\alpha_A-\alpha_C$			67		
Tyr157 O^{η} (τ_B)↔Asp202 O^{δ} (α_C)	$\alpha_A-\alpha_C$		32	52	100	82
Tyr157 O^{η} (τ_B)↔Glu196 O^{ϵ} (τ_D)	$\alpha_A-\alpha_C$	82				13
Asn159 N^{δ} (τ_B)↔Ala133 O	α_A			9	1	73
Tyr162 N (β_B)↔Thr183 O^{γ} (α_B)	$\beta-\alpha_{BC}$	7	88	77	34	97
Thr163 O^{η} (β_B)↔Ser222 O^{γ} (α_C)	$\beta-\alpha_{BC}$				70	
Arg164 N^{η} (τ_C)↔Asp178 O^{δ} (α_B)	$\beta-\alpha_{BC}$	99	4	24	89	90
Asn171 N^{δ} (τ_C)↔Glu168 O^{ϵ} (τ_C)	$\tau\pm4$			64	91	8
Thr183 O^{γ} (α_B)↔Cys179 O (α_B)	$\alpha\pm4$	58		100	100	100
His187 N^{ϵ} (α_B)↔Gln160 O (τ_B)	$\beta-\alpha_{BC}$					45
His187 N^{ϵ} (α_B)↔Met206 O (α_C)	α_{BC}			30	42	
Thr188 O^{γ} (α_B)↔Ile184 O (α_B)	$\alpha\pm4$	100		100	100	93
Thr191 O^{γ} (α_B)↔His187 O (α_B)	$\alpha\pm4$			100	94	45
Thr199 N (τ_D)↔Asp202 O^{δ} (α_C)	$\alpha\pm4$	1	56	11	24	93
Arg208 N^{η} (α_C)↔Glu146 O^{ϵ} (α_A)	$\alpha_A-\alpha_C$	59		92	98	99
Gln212 N^{ϵ} (α_C)↔Arg208 O (α_C)	$\alpha\pm4$	2	4	29	45	38
Ser222 O^{γ} (α_C)↔Tyr218 O (α_C)	$\alpha\pm4$	74		99	82	97

[a] The secondary structure elements, corresponding to the NMR structure of *Sh*PrP(90−231) (*29*), are shown in parentheses. Underlined residues are those for which mutation is associated with CJD, GSS, or FFI in humans. $\alpha\pm4$ and $\tau\pm4$ mark H-bonds involving neighboring residues in α-helical structures and in turns, respectively. $\alpha_A-\alpha_C$, $\beta-\alpha_{BC}$, and α_{BC} denote H-bonds between secondary structure elements and α_A H-bonds within the corresponding structure elements (see text for detailed description). [b] Calculated from the 25 conformations in PDB 1B10 (*29*).

corresponding to mutations. During the simulation of the *Hu*PrP model the number of exposed charged residues changed slightly, to six Lys, six Arg, five His, four Glu, and four Asp, caused mainly by small conformational changes in the regions of helix A and turn D, and turn C and turn A, and leading to two additional salt bridges. Despite a large total number of charged residues on the surface of PrP, the N-terminal part of the PrP model, 90−126, does not have any negatively charged residues but instead has four Lys and two His residues. Helix A (144−152), on the other hand, has a highly charged surface with Asp144, Glu146, Asp147, Arg148, Arg151, and Glu152. His155 and Arg156 on the nearby turn B increase the local charge potential. In contrast, the most conserved sequence region among all PrPs, PrP(113−127), has no charged or polar residues. Taken together, this makes PrP a protein which has different regions with distinctively different electrostatic properties.

The AMBER94 force field (*57*) is based on charges from ab initio calculations in gas phase, leading to partial charges which are generally higher than those from other force fields. Consequently, in simulations of highly charged systems, such as DNA and RNA (*48*) or proteins such as PrP, with the AMBER force field, a correct treatment of the electrostatic interactions appears to be even more necessary to get stable trajectories. Using a truncation method for the electrostatic interactions introduces artificial forces and leads to unstable trajectories. These artificial forces are reflected in an increase in the system temperature, which in itself is not responsible for the instability, as shown by the test simulation at 320 K using the PME method. As reported for other systems (*54*), salt ion concentration affects the stability of trajectories in simulations using the PME method, even though most of the salt ions are not interacting with the protein but are dispersed in the solvent. Secondary structures, in particular α-helical structures, show higher stability for simulations with the ionic models *Hu*PrP−Na and *Hu*PrP−Ca, whereas in the simulation with the minimum number of salt ions (*Hu*PrP−Cl), helices A and C break up significantly. Introduction of Ca^{2+} divalent cations into the system appears neither to increase distortion nor to make the structure more stable. The four sites of strong ion−protein interaction, for which the two negatively charged residues in close proximity were the original reason for introducing the Ca^{2+} ions, are occupied in both models by corresponding cations throughout the simulation. Only one of these sites, at Glu211, might have an effect on the structure, as in both models, *Hu*PrP−Na and *Hu*PrP−Ca, helix C shows a split at the nearby Gln212 and Met213 residues. Interestingly, mutation of Gln212 into Pro, which might disturb the α-helical structure, is also known to be associated with GSS in humans (*13*). On the other hand, while the NMR structure of *Mo*PrP(121−231) also shows a split of helix C, this is at position 220−221 (*26*). The MD simulations generally show shortened α-helical structure compared with the NMR structures and might, therefore, still represent somewhat deficient PrP models.

*Hu*PrP has one disulfide bridge between helix B and helix C, which stabilizes the three-dimensional structure of the

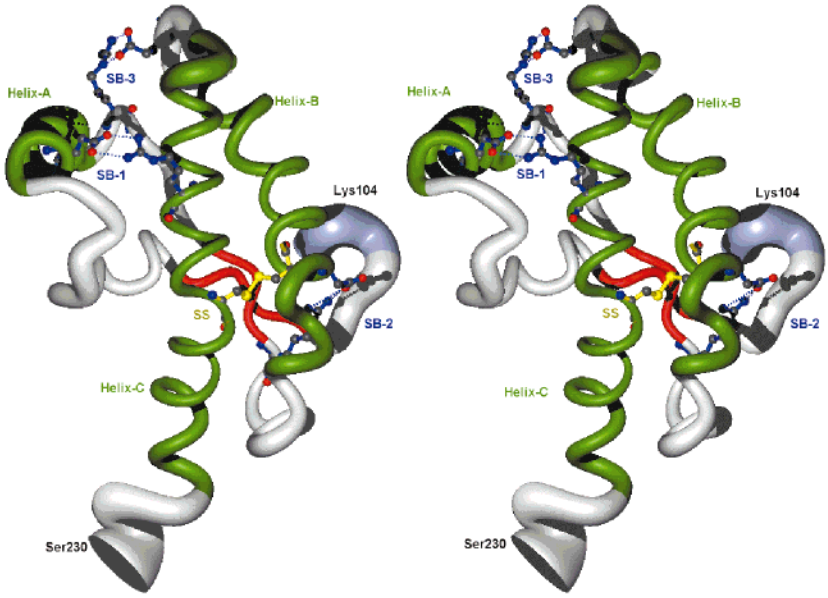

FIGURE 9: Stereoview of the average structure of *Hu*PrP from the *Hu*PrP−Na simulation using the PME method for the electrostatic interactions. The structure, including only the *Hu*PrP from Lys104 to Ser230, is shown as a coil of the Cα trace, where the thickness of the coil represents the fluctuation of the Cα atoms. The thicker the coil, the more flexible the structure in the simulation. Helical regions are in green and the β-strand region is in red. Also shown are the disulfide bridge (Cys179−Cys214, SS) in yellow and the three major salt bridges, Glu146↔Arg208 (SB-1), Arg164↔Asp178 (SB-2), and Arg156↔Glu196 (SB-3), in blue. The picture was generated using MOLMOL (*66*) and POVRAY (http://www.povray.org).

protein. In addition, three highly occupied salt bridges have been identified in the simulations of the *Hu*PrP and *Sh*PrP models, one between helix A and helix C (Glu146/Asp144↔Arg208), one between strand B (Arg164) and helix B (Asp178), and one between turn B (Arg156) and turn D (Glu196). Figure 9 shows these three salt bridges mapped onto the average backbone structure of the *Hu*PrP−Na model. Two of these salt bridges include residues for which mutation is associated with CJD or FFI in humans, Arg208→His and Asp178→Asn (*3*). Loss of these salt bridges may loosen the structure of PrP and facilitate a conformational change to the protease-resistant PrP^{Sc} conformation. These salt bridges fix the distance between the stable main *structured* core of *Hu*PrP, helix B and helix C, to the more flexible *structured* part, helix A and strands A and B. The distance between these two regions is further constrained by H-bonds, such as Tyr157 O^{η}↔Asp202 O^{δ} and Tyr162 N↔Thr183 O^{γ}. The latter H-bond involves Thr183, for which mutation into Ala is associated with disease in humans (*3*). However, this mutation also prevents *N*-glycosylation at Asn181 leading to intracellular accumulation of PrP (*72*, *73*). Mutation of Asp202→Asn is also known to be disease-associated (*13*), but the Asn residue retains its H-bond ability. The third highly occupied salt bridge, Arg156↔Glu196, involves two more flexible turn regions. One of the two residues, Arg156, is at the end of a 3_{10}-helical region, which forms a C-terminal extension of helix A. In summary, it appears that for PrP the electrostatic interactions, in general, and the salt bridges, in particular, play an important role. The fact that the simulation stability of PrP is strongly dependent on correct treatment of the electrostatic interactions is internally consistent with the fact that the highly occupied salt bridges found in the simulations involve residues for which mutations are known to be associated with disease in humans and for which such mutation would prevent formation of two of the salt bridges. While the residues involved in the three salt bridges are highly conserved in mammalian and marsupial PrPs, no diseases are known so far in these species, other than humans (*74*), which involve a mutation of one of these residues. The chicken PrP has an amino acid sequence which might allow equivalent salt bridges between 156↔202 and 164↔178 but not between 146↔208 and 156↔196. The H-bond network, on the other hand, does not seem to have such a stabilizing effect on the tertiary structure of PrP, as no major H-bonds could be identified which involve residues for which mutation is associated with disease in humans.

PrP^{C}, in its physiological role, cycles between the cell membrane and endosomic particles (*8*, *9*), presenting different electrostatic environments (different pHs) to PrP. The *Hu*PrP models were simulated in a protonation state corresponding to a pH value of 7, which is similar to an extracellular environment. Both NMR structures, *Sh*PrP and *Mo*PrP, were determined at pH values lower than 7 [*Sh*PrP at pH 5.2 (*29*) and *Mo*PrP at 4.5 (*23*)] and even lower than the environment in endosomic particles [pH 6.0−6.3 (*75*)]. These different pH values may be the underlying reason for the differences in the salt bridge structure between the NMR experiments (with one salt bridge for *Sh*PrP and two salt bridges for *Mo*PrP) and the simulations (three salt bridges). In addition, the disease-associated form of PrP (PrP^{Sc}) accumulates in late endosomes or lysosomes, which have an even more acidic environment (pH ∼4). Differences in salt bridge structure at different pH values or different environments might, therefore, have physiological relevance for PrP not only during normal recycling but also during abnormal disease-associated recycling or accumulation.

Several studies have been published on the guanidinium hydrochloride (Gdn-HCl) or temperature-induced unfolding of PrPs (*76*−*84*). Even though the results vary somewhat for the number of folding transition states, they all agree that a low pH value increases the instability or the unfolding

properties. At a pH value lower than 6, human PrP (*81*, *83*), mouse PrP (*82*), and hamster PrP (*80*) show a greater rate of Gdn-HCl induced unfolding and, additionally, show transition states with a high content of β-sheet structure. Also, mutation of amino acids involved in salt bridges we found showed a decreased PrP stability, leading to an increased free energy of unfolding $\Delta\Delta G°_{fold}$ (mutant − wild type) of 7.2−8.0 kJ/mol for the Asp178→Asn mutation and of 6.0 kJ/mol for the Arg208→Lys mutation (*84*). These findings are all consistent with our suggestion that salt bridges are involved in the stabilization of PrP and that elimination of such salt bridges, due to protonation of the acidic amino acids at low pH or by mutation of relevant amino acids, decreases the stability of PrP.

The NMR studies of PrP showed that most of the PrP structure is highly flexible and, hence, no structural assignment could be made for these regions. Although the *Sh*PrP NMR experiments revealed some interaction of the highly conserved *hydrophobic* part (PrP112−131) with the *structured* part of PrP, no structure could be assigned (*29*). The simulations, on the other hand, indicated some tendency of this *hydrophobic* part before strand A to form an α-helical or, at least, 3_{10}-helical conformation. Although this result agrees to some extent with some of the NMR experiments showing a weak Cα shift corresponding to α-helical conformation (*25*), the helical conformation is dynamically unstable, occurring only up to 40% of the simulation time in the case of the *Sh*PrP−Na model, and clarification of this issue would require additional investigations by MD simulations.

In summary, it has been shown that for a protein, such as PrP, with a large number of charged residues on the surface, MD simulations need to include correct treatment of the electrostatic interactions. Salt ions appear to have an additional stabilizing effect, especially for α-helical structure, but divalent cations produce no further stabilization advantage. From the MD simulations of *Hu*PrP three highly occupied salt bridges could be identified, which seem to be important for the stability of PrP. Mutations of residues involved in some of these salt bridges are known to be associated with diseases in humans.

ACKNOWLEDGMENT

We are grateful to the Australian National University Supercomputer Facility for providing computer time on the SGI and VPP supercomputers and to Dr. Thomas Huber for providing the optimized SANDER version of AMBER 5.0 for the VPP supercomputer and assisting on technical and scientific questions.

REFERENCES

1. Prusiner, S. B. (1996) in *Fields Virology* (Fields, B. N., Knipe, D. M., and Howley, P. M., Eds.) pp 2901−2950, Lippincott-Raven, Philadelphia, PA.
2. Edenhofer, F., Weiss, S., Winnacker, E. L., and Famulok, M. (1997) *Angew. Chem., Int. Ed. Engl. 36*, 1675−1694.
3. Ironside, J. W. (1998) *J. Pathol. 186*, 227−234.
4. Prusiner, S. B. (1991) *Science 252*, 1515−1522.
5. Cohen, F. E., and Prusiner, S. B. (1998) *Annu. Rev. Biochem. 67*, 793−819.
6. Pan, K. M., Baldwin, M., Nguyen, J., Gasset, M., Serban, A., Groth, D., Mehlhorn, I., Huang, Z., Fletterick, R. J., Cohen, F. E., and Prusiner, S. B. (1993) *Proc. Natl. Acad. Sci. U.S.A. 90*, 10962−19666.
7. Horwich, A., and Weissman, J. (1997) *Cell 89*, 499−510.
8. Shyng, S. L., Huber, M. T., and Harris, D. A. (1993) *J. Biol. Chem. 268*, 15922−15928.
9. Vey, M., Pilkuhn, S., Wille, H., Nixon, R., DeArmond, S. J., Smart, E. J., Anderson, R. G., Taraboulos, A., and Prusiner, S. B. (1996) *Proc. Natl. Acad. Sci. U.S.A. 93*, 14945−14949.
10. Arnold, J. E., Tipler, C., Laszlo, L., Hope, J., Landon, M., and Mayer, R. J. (1995) *J. Pathol. 176*, 403−411.
11. Barbanti, P., Fabbrini, G., Salvatore, M., Petraroli, R., Cardone, F., Maras, B., Equestre, M., Macchi, G., Lenzi, G. L., and Pocchiari, M. (1996) *Neurology 47*, 741−750.
12. Samaia, H. B., Mari, J. J., Vallada, H. P., Moura, R. P., Simpson, A. J., and Brentani, R. R. (1997) *Nature 390*, 241.
13. Piccardo, P., Dlouhy, S. R., Lievens, P. M., Young, K., Bird, T. D., Nochlin, D., Dickson, D. W., Vinters, H. V., Zimmerman, T. R., MacKenzie, I. R., Kish, S. J., Ang, L. C., De Carli, C., Pocchiari, M., Brown, P., Gibbs, C. J., Jr., Gajdusek, D. C., Bugiani, O., Ironside, J., Tagliavini, F., and Ghetti, B. (1998) *J. Neuropathol. Exp. Neurol. 57*, 979−988.
14. Cervenakova, L., Buetefisch, C., Taller, I., Lee, H.-S., Stone, G., Gibbs, C. J. J., Brown, P., Hallett, M., and Goldfarb, L. G. (1999) *J. Med. Genet.* (in press).
15. Eigen, M. (1996) *Biophys. Chem. 63*, A1−A18.
16. Jarrett, J. E., and Lansbury, P. T. J. (1993) *Cell 73*, 1055−1058.
17. Stahl, N., Borchelt, D. R., Hsiao, K., and Prusiner, S. B. (1987) *Cell 51*, 229−240.
18. Stahl, N., Baldwin, M. A., Hecker, R., Pan, K. M., Burlingame, A. L., and Prusiner, S. B. (1992) *Biochemistry 31*, 5043−5053.
19. Baldwin, M. A., Burlingame, A. L., and Prusiner, S. B. (1993) *Trends Anal. Chem. 12*, 239−248.
20. Haraguchi, T., Fisher, S., Olofsson, S., Endo, T., Groth, D., Tarentino, A., Borchelt, D. R., Teplow, D., Hood, L., Burlingame, A., Lycke, E., Kobata, A., and Prusiner, S. B. (1989) *Arch. Biochem. Biophys. 274*, 1−13.
21. Endo, T., Groth, D., Prusiner, S., and Kobata, A. (1989) *Biochemistry 28*, 8380−8388.
22. Stimson, E., Hope, J., Chong, A., and Burlingame, A. L. (1999) *Biochemistry 38*, 4885−4895.
23. Riek, R., Hornemann, S., Wider, G., Billeter, M., Glockshuber, R., and Wuthrich, K. (1996) *Nature 382*, 180−182.
24. Billeter, M., Riek, R., Wider, G., Hornemann, S., Glockshuber, R., and Wuthrich, K. (1997) *Proc. Natl. Acad. Sci. U.S.A. 94*, 7281−7285.
25. Riek, R., Hornemann, S., Wider, G., Glockshuber, R., and Wuthrich, K. (1997) *FEBS Lett. 413*, 282−288.
26. Riek, R., Wider, G., Billeter, M., Hornemann, S., and Glockshuber, R. (1998) *Proc. Natl. Acad. Sci. U.S.A. 95*, 11667-1172.
27. James, T., Liu, H., Ulyanov, N., Farr-Jones, S., Zhang, H., Donne, D., Kaneko, K., Groth, D., Mehlhorn, I., Prusiner, S., and Cohen, F. (1997) *Proc. Natl. Acad. Sci. U.S.A. 94*, 10086−10091.
28. Donne, D. G., Viles, J. H., Groth, D., Mehlhorn, I., James, T. L., Cohen, F. E., Prusiner, S. B., Wright, P. E., and Dyson, H. J. (1997) *Proc. Natl. Acad. Sci. U.S.A. 94*, 13452−13457.
29. Liu, H., Farr-Jones, S., Ulyanov, N. B., Llinas, M., Marqusee, S., Groth, D., Cohen, F. E., Prusiner, S. B., and James, T. L. (1999) *Biochemistry 38*, 5362−5377.
30. van Gunsteren, W. F., and Berendsen, H. J. C. (1990) *Angew. Chem., Int. Ed. Engl. 29*, 992−1023.
31. Braatz, J. A., Paulsen, M. D., and Ornstein, R. L. (1992) *J. Biomol. Struct. Dyn. 9*, 935−949.
32. Fox, T., and Kollman, P. A. (1996) *Proteins 25*, 315−334.
33. Duan, Y., and Kollman, P. A. (1998) *Science 282*, 740−744.
34. Steinbach, P. J., and Brooks, B. R. (1994) *J. Comput. Chem. 15*, 667−683.
35. Loncharich, R. J., and Brooks, B. R. (1989) *Proteins 6*, 32−45.
36. Guenot, J., and Kollman, P. A. (1993) *J. Comput. Chem. 14*, 295−311.

37. Fritsch, V. G., Ravishanker, G., Beveridge, D. L., and Westhof, E. (1993) *Biopolymers 33*, 1537−1552.
38. Aveblj, F., Moult, J., Kitson, D. H., James, M. N. G., and Hagler, A. T. (1990) *Biochemistry 29*, 8658−8676.
39. York, D. M., Darden, T. A., Pedersen, L. G., and Anderson, M. W. (1993) *Biochemistry 32*, 1443−1453.
40. Marlow, G. E., Perkyns, J. S., and Pettit, B. M. (1993) *Chem. Rev. 93*, 2503−2521.
41. Yelle, R. B., Park, N. S., and Ichiye, T. (1995) *Proteins 22*, 154−167.
42. Marti-Renom, M. A., Mas, J. M., Oliva, B., Querol, E., and Aviles, F. (1998) *Protein Eng. 11*, 881−890.
43. Darden, T., York, D., and Pedersen, L. (1993) *J. Chem. Phys. 98*, 10089−10092.
44. Darden, T., Perera, L., Li, L., and Pedersen, L. (1999) *Structure 7*, R55−R60.
45. Cheatham, T. E. I., Miller, K. J., Fox, T., Darden, T. A., and Kollamn, P. A. (1995) *J. Am. Chem. Soc. 117*, 4193−4194.
46. York, D. M., Yang, W., Lee, H., Darden, T. A., and Pedersen, L. G. (1995) *J. Am. Chem. Soc. 117*, 5001−5002.
47. Young, M. A., Ravishanker, G., and Beveridge, D. L. (1997) *Biophys. J. 73*, 2313−2336.
48. Auffinger, P., and Westhof, E. (1997) *J. Mol. Biol. 269*, 326−341.
49. De Souza, O. N., and Ornstein, R. L. (1997) *Biophys. J. 72*, 2395−2397.
50. McConnell, K. J., Nirmala, R., Young, M. A., Ravishanker, G., and Beveridge, D. L. (1994) *J. Am. Chem. Soc. 116*, 4461−4462.
51. Li, L., Darden, T. A., Freedman, S. J., Furie, B. C., Furie, B., Baleja, J. D., Smith, H., Hiskey, R. G., and Pedersen, L. G. (1997) *Biochemistry 36*, 2132−2138.
52. Ibragimova, G. T., and Wade, R. (1998) *Biophys. J. 74*, 2906−2911.
53. Wrigger, W., Mehler, E., Pitici, F., Weinstein, H., and Schulten, K. (1998) *Biophys. J. 74*, 1622−1639.
54. Pfeiffer, S., Fushman, D., and Cowburn, D. (1999) *Proteins 35*, 206−217.
55. Pearlman, D. A., Case, D. A., Caldwell, J. W., Ross, W. S., Cheatham, T. E., DeBolt, S., Ferguson, D., Seibel, G., and Kollman, P. A. (1995) *Comput. Phys. Commun. 91*, 1−41.
56. Case, D. A., Pearlman, D. A., Caldwell, J. W., Cheatham, T. E., Ross, W. S., Simmerling, C. L., Darden, T. A., Merz, K. M., Stanton, R. V., Cheng, A. L., Vincent, J. J., Crowley, M., Ferguson, D. M., Radmer, R. J., Seibel, G. L., Singh, U. C., Weiner, P. K., and Kollman, P. A. (1997) *AMBER 5*, University of California, San Francisco.
57. Cornell, W. D., Cieplak, P., Bayly, C. I., Gould, I. R., Merz, K. M., Ferguson, D. M., Spellmeyer, D. C., Fox, T., Caldwell, J. W., and Kollman, P. A. (1995) *J. Am. Chem. Soc. 117*, 5179−5197.
58. Åqvist, J. (1990) *J. Phys. Chem. 94*, 8021−8024.
59. Sali, A., and Blundell, T. L. (1993) *J. Mol. Biol. 234*, 779−815.
60. Petersen, M. T., Martel, P., Petersen, E. I., Drablos, F., and Petersen, S. B. (1997) *Methods Enzymol. 284*, 130−154.
61. Hooft, R. W. W., Vriend, G., Sander, C., and Abola, E. E. (1996) *Nature 381*, 272.
62. Berendsen, H. J. C., Postma, J. O. M., van Gunsteren, W. F., DiNola, A., and Haak, J. R. (1984) *J. Chem. Phys. 81*, 3684−3690.
63. Kabsch, W., and Sander, C. (1983) *Biopolymers 22*, 2577−2637.
64. Kraulis, P. J. (1991) *J. Appl. Crystallogr. 24*, 946−950.
65. Bacon, D. J., and Anderson, W. F. (1988) *J. Mol. Graphics 6*, 219−220.
66. Koradi, R., Billeter, M., and Wüthrich, K. (1996) *J. Mol. Graphics 14*, 51−55.
67. Hünenberger, P. H., and McCammon, J. A. (1999) *J. Chem. Phys. 110*, 1856−1872.
68. Hünenberger, P. H., and McCammon, J. A. (1999) *Biophys. Chem. 78*, 69−88.
69. Strynadka, N. C. J., and James, M. N. G. (1989) *Annu. Rev. Biochem. 58*, 951−998.
70. Gebe, J. A., Delrow, J. J., Heath, P. J., Fujimoto, B. S., Stewart, D. W., and Schurr, J. M. (1996) *J. Mol. Biol. 262*, 105−128.
71. Sprous, D., Young, M. A., and Beveridge, D. L. (1999) *J. Mol. Biol. 285*, 1623−1632.
72. Rogers, M., Taraboulos, A., Scott, M., Groth, D., and Prusiner, S. B. (1990) *Glycobiology 1*, 101−109.
73. Lehmann, S., and Harris, D. A. (1997) *J. Biol. Chem. 272*, 21479−21487.
74. Prusiner, S. B. (1997) *Science 278*, 245−250.
75. Maxfield, F., and Mayor, S. (1997) *Adv. Exp. Med. Biol. 419*, 355−364.
76. Safar, J., Roller, P. P., Gajdusek, D. C., and Gibbs, C. J., Jr. (1993) *Protein Sci. 2*, 2206−2216.
77. Safar, J., Roller, P. P., Gajdusek, D. C., and Gibbs, C. J., Jr. (1994) *Biochemistry 33*, 8375−8383.
78. Kocisko, D. A., Lansbury, P. T. J., and Caughey, B. (1996) *Biochemistry 35*, 13434−13442.
79. Hornemann, S., and Glockshuber, R. (1996) *J. Mol. Biol. 261*, 614−619.
80. Zhang, H., Stockel, J., Mehlhorn, I., Groth, D., Baldwin, M., Prusiner, S., James, T., and Cohen, F. (1997) *Biochemistry 36*, 3543−3553.
81. Swietnicki, W., Petersen, R., Gambetti, P., and Surewicz, W. K. (1997) *J. Biol. Chem. 272*, 27517−27520.
82. Hornemann, S., and Glockshuber, R. (1998) *Proc. Natl. Acad. Sci. U.S.A. 95*, 6010−6014.
83. Jackson, G. S., Hill, A. F., Joseph, C., Hosszu, L., Power, A., Waltho, J. P., Clarke, A. R., and Collinge, J. (1999) *Biochim. Biophys. Acta 1431*, 1−13.
84. Liemann, S., and Glockshuber, R. (1999) *Biochemistry 38*, 3258−3267.

BI991469D